ZT Enhancement in Solution-Grown $Sb_{(2-x)}Bi_xTe_3$ Nanoplatelets

Marcus Scheele,[†,*] Niels Oeschler,[‡] Igor Veremchuk,[‡] Klaus-Georg Reinsberg,[§] Anna-Marlena Kreuziger,[†] Andreas Kornowski,[†] José Broekaert,[§] Christian Klinke,[†] and Horst Weller[†]

[†]University of Hamburg, Institute of Physical Chemistry, Grindelallee 117, 20146 Hamburg, Germany, [‡]Max Planck Institute of Chemical Physics of Solids, Noethnitzer Strasse 40, 01187 Dresden, Germany, and [§]University of Hamburg, Institute of Inorganic and Applied Chemistry, Martin-Luther-King-Platz 6, 20146 Hamburg, Germany

ABSTRACT We report a solution-processed, ligand-supported synthesis of 15−20 nm thick $Sb_{(2-x)}Bi_xTe_3$ nanoplatelets. After complete ligand removal by a facile NH_3-based etching procedure, the platelets are spark plasma sintered to a p-type nanostructured bulk material with preserved crystal grain sizes. Due to this nanostructure, the total thermal conductivity is reduced by 60% in combination with a reduction in electric conductivity of as low as 20% as compared to the bulk material demonstrating the feasibility of the phonon-glass electron-crystal concept. An enhancement in the dimensionless thermoelectric figure of merit of up to 15% over state-of-the-art bulk materials is achieved, meanwhile, shifting the maximum to significantly higher temperatures.

KEYWORDS: nanostructured solids · thermoelectrics · colloids · thermal conductivity · phonon-glass electron-crystal

Recently, Bi_2Te_3-based nanostructured materials have received great attention due to their outstanding thermoelectric properties. From the first reports in the 1950s until today, the dimensionless thermoelectric figure of merit (ZT) of such materials at room temperature has been improved 3-fold. From 0.5 for pure Bi_2Te_3 bulk samples over 1.14 for bulk $(Bi_2Te_3)_{0.25}(Sb_2Te_3)_{0.72}(Sb_2Se_3)_{0.03}$ and 1.2 for nanostructured BiSbTe alloys to 1.56 for nanostructured $Sb_{1.52}Bi_{0.48}Te_3$ with "*coherent interfaces*", advances in semiconductor manipulation have yielded impressive results in this ecologically highly promising field.[1−4] ZT is estimated to require a value of 3 to be competitive with conventional cooling devices and to open up novel pathways for efficient and greener power generation.

The record high efficiency of 2.4 was reported for molecular beam epitaxy engineered thin films of Bi_2Te_3/Sb_2Te_3 layers, which may be difficult to use in large-scale applications but convincingly demonstrated the potential for further improvements to come from nanostructured Bi_2Te_3-based materials.[5]

To fabricate such materials on a macroscopic scale, one conventionally applies high pressure and suitable temperatures to sinter a Bi_2Te_3 based nanopowder to a dense nanocomposite with preserved crystal grain boundaries. Such nanocomposites have been studied by the means of transmission electron microscopy (TEM), energy dispersive X-ray spectroscopy (EDXS), and scanning electron microscopy (SEM).[6,7] It is believed that the unique structural details in these materials such as laminated structure, coherent interfaces, nanoprecipitates with defect concentrations, and broad size distribution of crystalline domains effect all three parameters of ZT, namely, the thermopower, electric, and thermal conductivity, and can lead to an overall improvement of thermoelectric efficiency.

Synthetic strategies to Bi_2Te_3-based nanopowders can be divided into two approaches: (a) ligandless or (b) ligand-supported nanograin growth. Advantages of the former are the absence of organic impurities and the good alloying possibilities by standard semiconductor manipulations. As a matter of this, the ligandless approach was more successful recently and all of the milestone achievements in enhancing ZT as cited above were due to this strategy. Methods of choice are techniques like ball-milling of ingots and melt-spinning.[3,4] An instructive summary has been provided recently by Ren and co-workers.[8] However, it is found to be almost impossible to achieve a good size control and narrow size distribution of nanoparticles by this strategy. This is the major advantage of solution processed, ligand supported nanoparticle growth strategies. Significantly better size control as compared to ligandless approaches has been achieved for a variety

*Address correspondence to scheele@chemie.uni-hamburg.de.

Received for review April 25, 2010 and accepted June 16, 2010.

10.1021/nn1008963

of high performance thermoelectric materials including Bi_2Te_3 and $Sb_{(2-x)}Bi_xTe_3$.[7,9] Majumdar and co-workers have shown that self-assembled colloidal PbSe nanoparticles synthesized in solution show an enhanced thermopower due to sharp spikes in the density of states because of quantum confinement effects.[10] We have reported recently a procedure capable of completely removing the ligand sphere of formally organically protected nanocrystals.[11] Thus treated, nanoparticles sintered to a macroscopic composite show the same electric conductivity as the bulk material. This tool in combination with the advances in solution processed nanotechnology opens up pathways to thermoelectric studies of nanocomposites with grain sizes where low-dimensional effects are really prominent that is drastically below 100 nm. Only when size and size-distribution of nanoparticles are small, one can obtain detailed insight into the change in thermoelectric parameters due to the limited dimensions. In the recent past, a growing number of theoreticians have turned to modeling the thermoelectric properties of such nanogranular composites, including the thermoelectric coefficient and figure of merit, transport properties, and the power factor.[12−14] Their results suggest that nanogranular materials not only display the easily understood decrease in lattice thermal conductivity, but also alterations in transport properties that are not as straightforward to comprehend as the influence on phonon transport. For the ongoing discussion to advance, new systems need to be designed to deliver experimental data for comparison with theoretical predictions. In this respect, ligand-supported growth of nanostructures provides an additional tool to access new and complex thermoelectric materials, which are difficult to obtain by conventional top-down approaches. Specifically, the synthesis of ultrathin Bi_2Te_3-based nanostructures has received great attention owed to the quickly evolving field of topological insulators.[15] As such, these structures have been synthesized by the means of the elemental reactant technique, exfoliation, and vapor-solid growth.[16−18] These techniques allow for much better control of the nanostructures' thickness than the top-down approaches mentioned above. However, the absolute yield is usually too low to fabricate macroscopic samples of it.

Here we report the large scale synthesis of $Sb_{(2-x)}Bi_xTe_3$ nanoplatelets in solution, their purification from organic ligands, the fabrication of macroscopic nanocomposites, and their full thermoelectric characterization.

RESULTS AND DISCUSSION

$Sb_{(2-x)}Bi_xTe_3$ nanoplatelets are synthesized similarly to a previously developed protocol for Bi_2Te_3 nanoparticles.[11] The acetates of Bi^{3+} and Sb^{3+} are treated with excess 1-dodecanethiol (DDT) under vacuum to remove acetic acid and form the metal thiolates that are easily soluble in organic media. Injecting the mild reducing agent oleylamine into this solution exclusively initiates the formation of a bismuth(0) species, referred to in the following as "*slow reduction*". Adding a solution of tellurium in trioctylphosphine (Te@TOP) within minutes after initiating the slow reduction triggers a much faster reduction by the more potent reducing agent trioctylphosphine (TOP). The metal(0) species formed during the "*fast reduction*" is unstable in the presence of the tellurium complex and reacts to the ternary antimony−bismuth−telluride compound. Shortly after beginning the fast reduction under these conditions, thin nanostructures only few nanometers in thickness of Sb−Bi−Te can be found, referred to in the following as "nanoflakes" (see Supporting Information, Figure S1). If kept at moderate temperatures (60 °C), the nanoflakes will combine to larger structures, referred to in the following as "nanosheets". During this process, the thickness of the sheets does not change significantly. Over time, an increasing number of defined geometric features like sharp edges, corners, and even symmetric hexagons is observed. Typically, the dimensions of the final nanosheets are 50−200 nm across and up to 5 nm in thickness as estimated by X-ray powder diffraction (XRPD) measurements. By increasing the reaction temperature (90 *vs* 60 °C), the thin and often porous nanosheets grow in thickness by the uptake of Sb_2Te_3 from the solution. The nanostructures resulting from this process are single-crystalline, 15−20 nm in thickness and will be referred to in the following as "nanoplatelets".

In Figure 1, transmission electron microscopy (TEM) reveals the shape of typical nanosheets (a) and nanoplatelets (b). A high resolution (HR-TEM) image (c) verifies the discontinuous nature of the nanosheets with the amorphous carbon substrate visible underneath. It is noteworthy that the whole sheet appears to be almost single-crystalline, which is further studied in Figure 1e. Here, the fast Fourier transform (FFT) of the image displays a clear atomic ordering, however, with a slight directional misalignment of the individual crystalline domains. From this it is inferred that the porous nanosheets evolve from nanoflakes throughout the course of the reaction. During this process, the individual nanoflakes have to align perfectly in one crystalline direction to eventually form a single crystal. The crystal depicted in the inset of Figure 1c is therefore an intermediate stage in this process. In contrast, the thicker nanoplatelets are continuous and perfectly single-crystalline (see Figure 1d). They are believed to develop from nanosheets of similar diameter by growing in thickness.

As visible in the FFT of the HR-TEM image (Figure 1e,f), the direction of growth of the sheets and platelets is in the *a*,*b*-plane, that is, along the [110] direction ([11-20] in Bravais annotation). This is a typical behavior of Bi_2Te_3 and Sb_2Te_3 owed to its highly anisotropic crys-

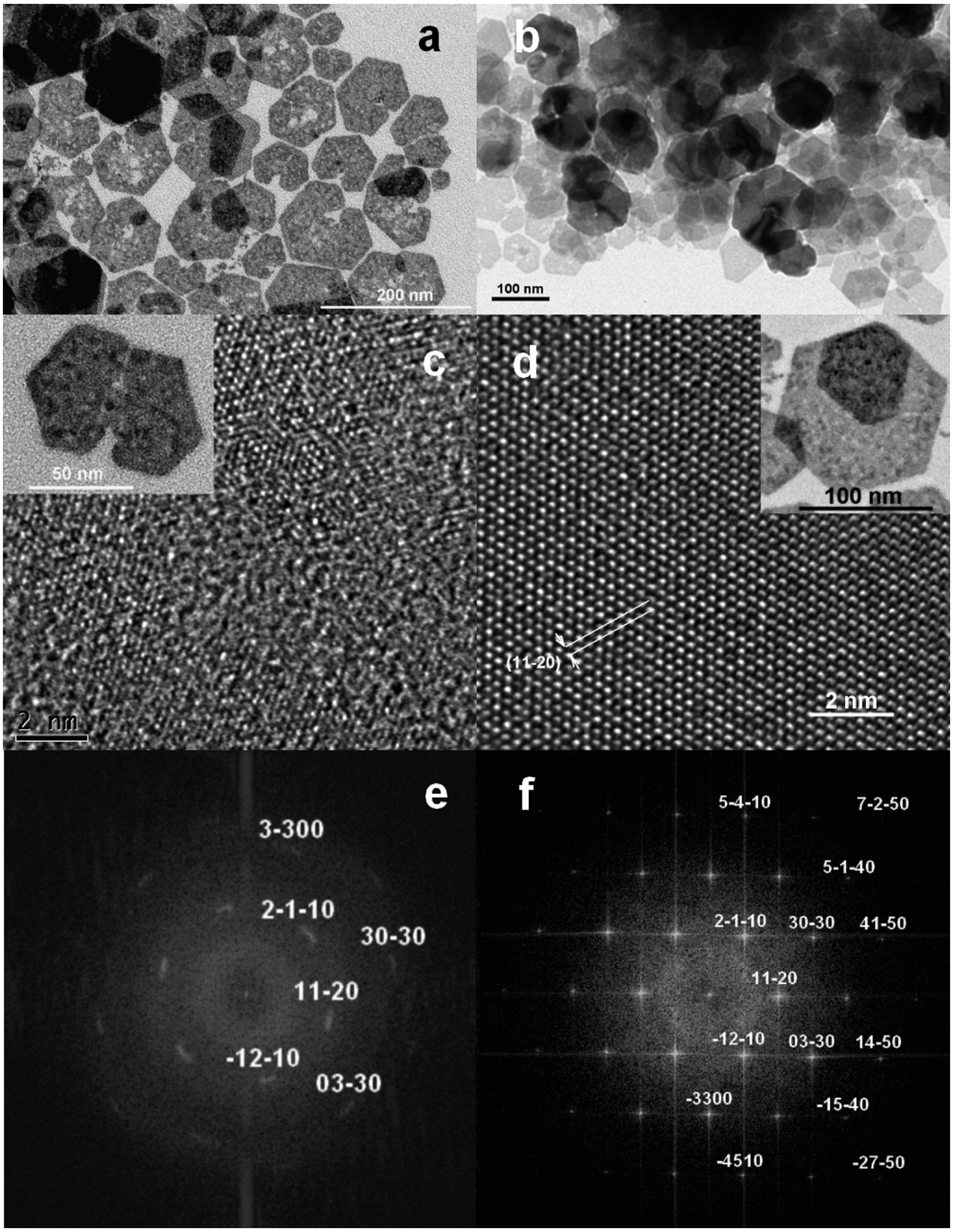

Figure 1. TEM images of $Sb_{(2-x)}Bi_xTe_3$ nanosheets (a) and nanoplatelets (b). HR-TEM images of individual (see inset) nanosheets (c) and nanoplatelets (d). The indicated lattice spacing is 2.15 Å, which corresponds to the spacing of (11-20) planes. Fast Fourier transformed of the HR-TEM images of nanosheets (e) and nanoplatelets (f). In each case, the direction of view is [0001].

tal structure.[19,20] For the evolution of platelets from sheets, an additional growth in the *c*-direction is required. The rate of this growth is too low at 60 °C so that even after 4 days of reaction only sheets are obtained. Increasing the temperature to 90 °C initiates growth in the *c*-direction and begins the formation of nanoplatelets.

Compositional analysis is shown in Figure 2 by the means of XRPD, energy dispersive X-ray spectroscopy (EDXS), and inductively plasma coupled optical emission spectroscopy (ICP-OES). The XRPD (Figure 2, left) of $Sb_{(2-x)}Bi_xTe_3$ nanoplatelets reveals a single-phase product with slightly broadened reflections typical for crystals with nanoscalic dimensions. Position and intensity of the reflections can be attributed to an intermediate of Bi_2Te_3 and Sb_2Te_3 with a Sb/Bi ratio much larger than unity. Lattice constants for a hexagonal unit cell were determined to $a = 4.268$ Å and $c = 30.40$ Å, which compares to 4.260/30.45 Å for pure Sb_2Te_3 and 4.38/30.48 Å for pure Bi_2Te_3. For comparison, an XRPD of nanosheets is displayed in the SI unit (Figure S2) revealing lattice constants of $a = 4.272$ Å and $c = 30.50$ Å.

EDXS and ICP-OES analysis (Figure 2, right) reveal antimony, bismuth and tellurium as the main constituting elements in the nanosheets and nanoplatelets. When comparing the quantitative elemental analysis

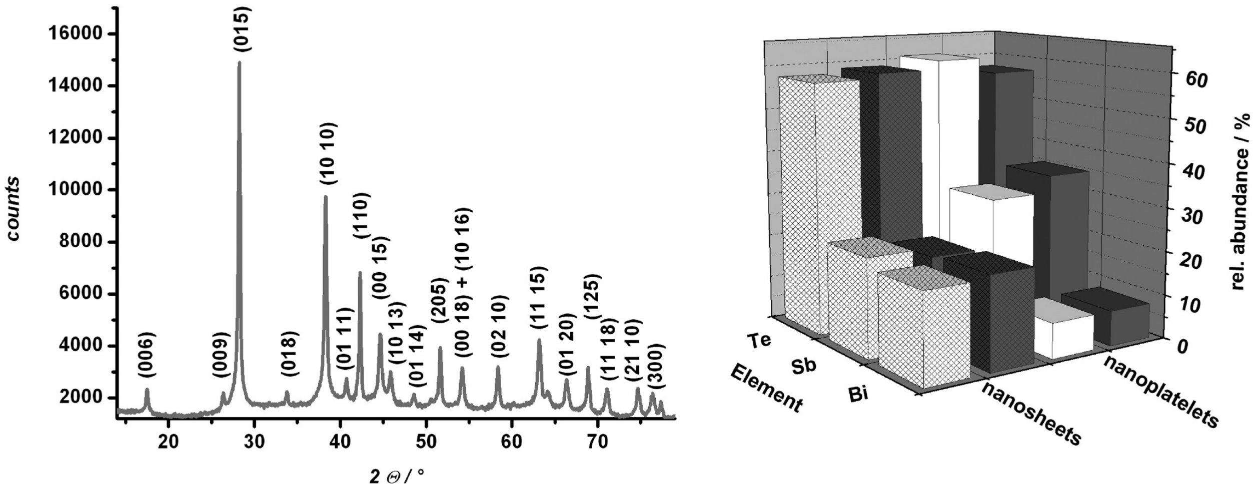

Figure 2. (Left) XRPD of $Sb_{(2-x)}Bi_xTe_3$ nanoplatelets with Sb/Bi ≈ 4:1. Indexing according to space group R-3*m* (166). (Right) Elemental analysis of $Sb_{(2-x)}Bi_xTe_3$ nanosheets (*hatched*) and nanoplatelets (*blank*). Individual nanocrystals were analyzed by EDXS (*light*), and large quantities of nanocrystal powder were analyzed by ICP-OES (*dark*).

of nanosheets and nanoplatelets it becomes evident that the $Sb_{(2-x)}Bi_xTe_3$ sheets have a much larger bismuth content (Sb/Bi ≈ 1:1, $Sb_{1.0}Bi_{1.0}Te_{3.0}$) than the platelets (Sb/Bi ≈ 4:1, $Sb_{1.7}Bi_{0.4}Te_{3.0}$). Note that optimized, bulk $Sb_{(2-x)}Bi_xTe_3$ usually has a Sb/Bi ratio of 3:1 ($Sb_{1.5}Bi_{0.5}Te_3$).[3] In both of the two structures the relative abundance of tellurium is always 57−59 at. %. The analytical results of individual nanosheets and platelets obtained by EDXS (see also Figure S3 in the SI unit) are in good agreement with the results of ICP-OES analysis of the same material subsequent to wet chemical digestion showing the homogeneity in chemical composition of the individual nanocrystals.

All organic residues are removed from the inorganic nanosheets or nanoplatelets to allow for high electric conductivities. Where solvents can be effectively withdrawn by multiple washing steps, the separation from the stabilizing agent DDT is realized by a modified procedure similar to a previously developed protocol.[11] As the only alteration, after ligand exchange with oleic acid we apply a methanolic NH_3 solution rather than hydrazine hydrate. The advantage is the nonreductive nature of NH_3 in comparison to the powerful reducing agent hydrazine. This way, an unwanted partial reduction of the nanosheets during the washing procedure can be excluded. After drying the inorganic material under vacuum, we obtain a dark-gray nanopowder. According to XRPD, this procedure has no significant impact on the crystalline phase of the nanomaterial (see SI, Figure S4).

To fabricate a nanostructured bulk material, this powder is spark plasma sintered (SPS) to a macroscopic pellet. Pellets of $Sb_{(2-x)}Bi_xTe_3$ nanosheets or nanoplatelets are silver−metallic in appearance with a density of 5.73 ± 0.10 g cm^{-3} (85% of theoretical density) under the conditions specified in the experimental section and SI unit (Figures S5, S6, and S7). To achieve larger densities toward 100% of the theoretical value, significantly higher sintering temperatures and duration are required, which resulted in unwanted grain growth during compaction.

In the following, we will focus on the thermoelectric properties of $Sb_{1.7}Bi_{0.4}Te_{3.0}$ nanoplatelets.

In Figure 3, the fine structure of the sintered pellets and its impact on the thermal conductivity is investigated. As displayed by SEM imaging in Figure 3a, the shape of individual nanoplatelets is preserved in the final pellets yielding a highly polycrystalline, layered material. We compare our thermal conductivity results with state-of-the-art macrocrystalline, bulk $Sb_{1.5}Bi_{0.5}T3_{3.0}$.[3] (Note: This reference mainly reported on nanostructured $Sb_{1.5}Bi_{0.5}Te_{3.0}$. In addition, it presented the complete thermoelectric characterization of a macrocrystalline sample for comparison. The values reproduced in the present work are those of the macrocrystalline sample.)

To calculate the total thermal conductivity (κ) from Laserflash measurements, we measured the specific heat (C_P, Figure 3b) repeatedly of several samples and on using three different measurement systems (Physical Property Measurement System by Quantum Design; Differential Scanning Calorimeter by Netzsch and Linseis). The deviation of all measurements was less than 5%. At 300 K we obtain C_P = 235 J kg^{-1} K^{-1}. Note that this is almost 25% higher than the Dulong-Petit limit for bulk materials. Such a deviation is typically observed for nanostructures and has been attributed to the large amount of surface atoms as compared to the total volume of these structures.[21−24] With this, an average density (ρ) of 5.73 g cm^{-3} and the thermal diffusivity results (D_t), we calculate the total thermal conductivity following the equation

$$\kappa = D_t \rho C_P \tag{1}$$

When measuring the transport properties of Bi_2Te_3-based compounds, great care must be taken about the

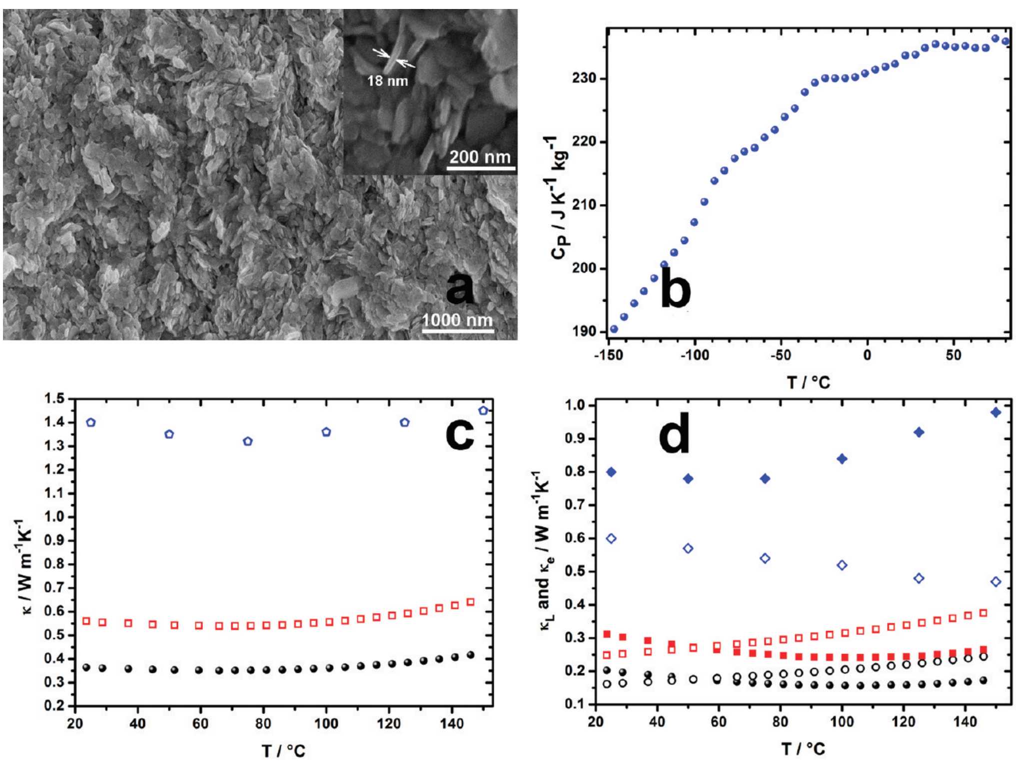

Figure 3. (a) SEM image of a spark plasma sintered pellet of $Sb_{1.7}Bi_{0.4}Te_{3.0}$ nanoplatelets. The inset contains a side view on individual nanoplatelets revealing their approximate thickness. (b) Specific heat capacity of a pellet of nanoplatelets. (c) Total thermal conductivity of nanoplatelets uncorrected (closed circles), corrected for porosity (open squares) and of a $Sb_{1.5}Bi_{0.5}Te_{3.0}$ bulk ingot taken from ref 3 (open diamonds). (d) Lattice ($κ_L$, closed) and electronic ($κ_e$, open) thermal conductivity of nanoplatelets uncorrected (circles), corrected for porosity (squares), and bulk ingots (diamonds).

individual measurement directions relative to the crystal's orientation. As Fleurial *et al.* have worked out, the anisotropy in thermal and electric transport between the *a*,*b*-plane and the *c*-axis of single-crystalline Bi_2Te_3 is 2−2.5.[25] A similar degree of transport anisotropy can be expected for single-crystalline $SbBiTe_3$. In pressed pellets of $SbBiTe_3$ nanoparticles, transport anisotropy depends on the degree of ordering of the individual nanocrystals in the pellet. As Ma *et al.* have shown, the random orientation of nanocrystals during hot-pressing can decrease transport anisotropy in nanostructured bulk $SbBiTe_3$ to less than 5%.[26] For the material presented in this work, we determined a temperature-dependent anisotropy in the thermal conductivity of 8−18%, with the lower thermal conductivity in the *c*-direction. (For details, see Supporting Information, Figure S8.) This anisotropy has been taken into account for all thermal conductivity measurements discussed below.

To allow a quantitative comparison of transport properties with 100% dense, bulk samples, it is important to account for the porosity of about 15% in the nanostructured samples presented in this work. As several groups have reported, porosity decreases thermal conductivity and electric conductivity alike.[27,28] Where the effect of porosity on ZT is usually small, if not negligible, individual transport parameters must be corrected for porosity to judge the effect of nanostructuring alone.[27] To do so, we follow Adachi *et al.* by using a Maxwell−Eucken expression[29]

$$x_P = x_0 \cdot \frac{1 - P}{1 + \beta P} \tag{2}$$

where *x* is either the thermal or the electric conductivity, x_P is the transport property in the porous medium, x_0 is the same property in the 100% dense medium, *P* is the degree of porosity (a fraction between 0 and 1), and β is an empirical parameter describing the shape of the pores. In the following, we set *P* to 0.15 and β to 2.0, which is a fair estimate related to similar works reported in literature.[29] Thus, the porosity in the material presented is estimated to account for a reduction in both, thermal and electric conductivity, to 65% of the theoretical value to be expected for an absolutely dense sample. Comparisons with other models accounting for the effects of porosity (e.g., the percolation model) verify this assumption to be very reasonable.[30,31] To display the pure effect of nanostructuring on the transport properties, we will use only the porosity corrected values in the following discussion. In Figures 3 and 4 we prefer to show both the uncorrected and corrected measurements for clarity.

The qualitative behavior of κ(*T*) of the pellets of nanoplatelets (Figure 3c) is similar to the bulk material insofar that the variation over the measurement range from 25 to 145 °C is less than 10% with a minimum at

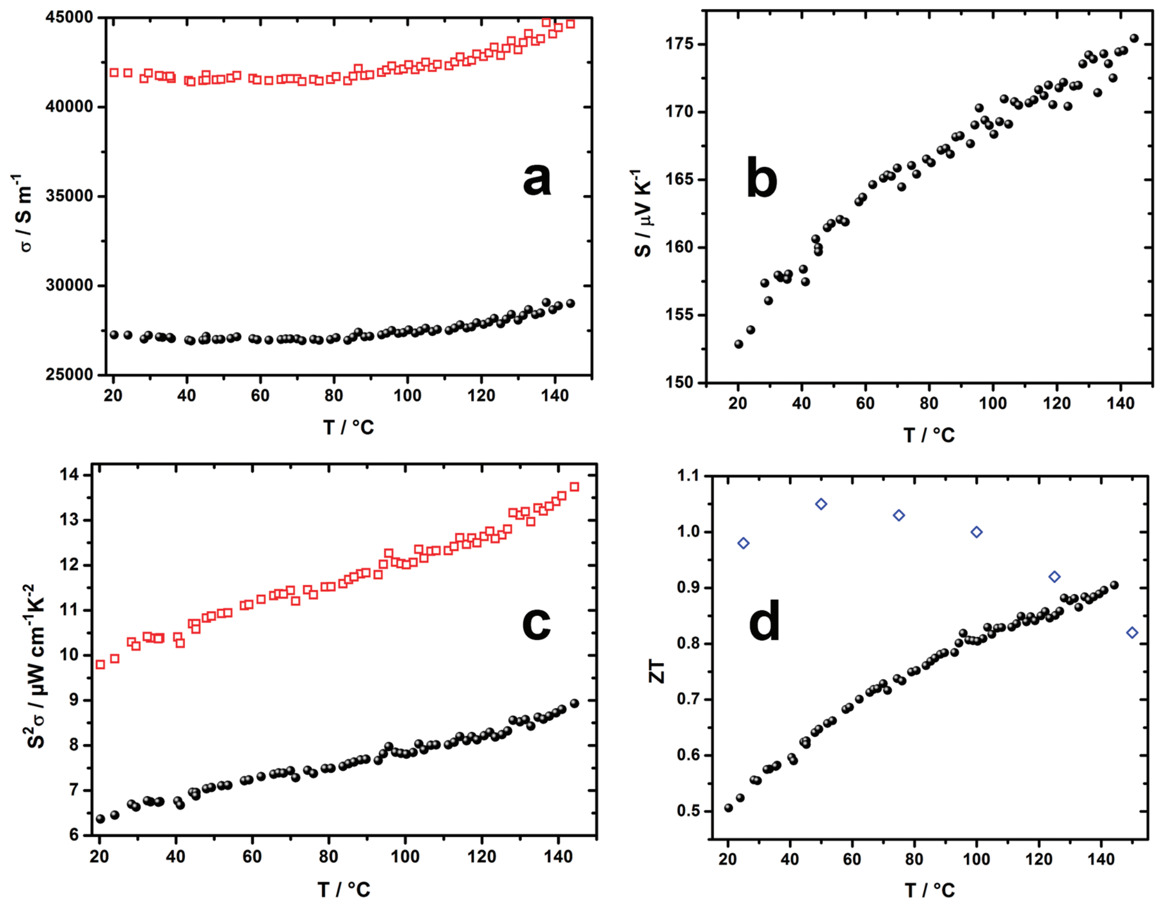

Figure 4. (a) Electric conductivity, (b) thermopower, (c) power factor, and (d) dimensionless figure of merit of a pellet of $Sb_{1.7}Bi_{0.4}Te_{3.0}$ nanoplatelets uncorrected (closed circles) and corrected for porosity (open squares). For comparison, the figure of merit of bulk $Sb_{1.5}Bi_{0.5}Te_{3.0}$ ingots is displayed (open diamonds).[3]

80 °C. With 0.56 W m^{-1} K^{-1} at 300 K, κ is 60% lower than that of a comparable bulk material.[3] As discussed below, some of this decrease results from a simultaneous decrease in electric conductivity (σ; see Figure 4), which overall has no effect on the thermoelectric figure of merit due to the Wiedemann−Franz law. Therefore, a more suitable measure to judge the potential of our material for improved thermoelectrics is the lattice part (κ_L) of the thermal conductivity. To calculate κ_L at a given temperature (T), we follow Tritt and co-workers and use $L = 2.0 \cdot 10^{-8}$ V^2 K^{-2}, which is accepted to be the appropriate value of the Lorentz number for heavily degenerated semiconductors.

$$\kappa_L = \kappa - \kappa_e = \kappa - L\sigma T \qquad (3)$$

With $\kappa_L = 0.31$ W m^{-1} K^{-1} at 300 K (Figure 3d), the decrease in phononic heat transport is again 60% with reference to the bulk material. It is worth mentioning that this value for κ_L is in excellent agreement with similar attempts to reduce phononic transport *via* nanostructuring by other groups.[3,4] Poudel *et al.* reported $\kappa_L = 0.34$ W m^{-1} K^{-1} and Xie *et al.* showed $\kappa_L = 0.26$ W m^{-1} K^{-1} (uncorrected for porosity of 4.5%).

Another important aspect in Figure 3d is the different behavior of $\kappa_L(T)$ and $\kappa_e(T)$. At room temperature, heat transport in the nanoplatelets is dominated by lattice vibrations, that is, $\kappa_L > \kappa_e$. With increasing T, this is reversed to $\kappa_L < \kappa_e$ due to improved electric transport. Quite the opposite behavior is known about bulk $Sb_{1.5}Bi_{0.5}Te_3$, where κ_e is always smaller than κ_L in this temperature regime.

In Figure 4, we display our σ (Figure 4a) and thermopower (S, Figure 4b) measurements, combine it to the power factor (σS^2, Figure 4c) and calculate the dimensionless figure of merit (ZT, Figure 4d) according to

$$ZT = \frac{\sigma S^2}{\kappa}T \qquad (4)$$

.

At room temperature, σ is decreased to 40% of the bulk value, which is the result of electron scattering at crystal grain boundaries. The large surface-to-volume ratio of nanograins results in high trap-state densities at each grain boundary caused by defects and dangling bonds. These trap-states immobilize charge carriers, leading to a reduced, effective mobility as compared to single crystals.[32] Furthermore, the grain boundaries become electrically charged and provide a grain boundary potential barrier to electric transport.[33] In contrast to bulk $Sb_{1.5}Bi_{0.5}Te_3$, the pellets of nanoplate-

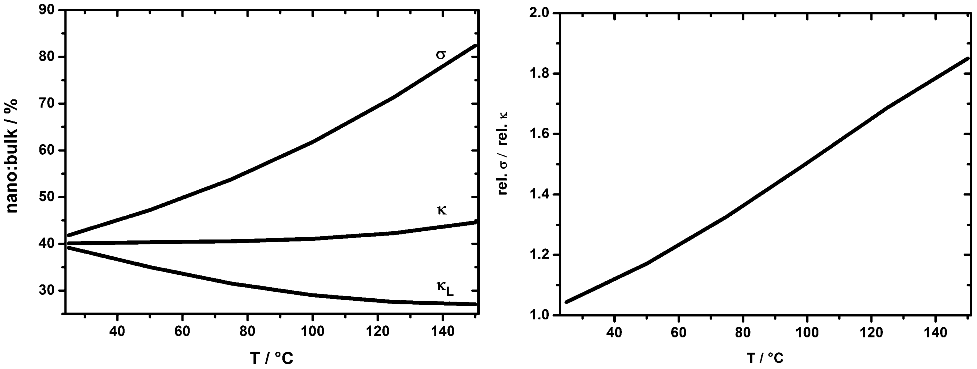

Figure 5. (Left) Relative decrease of transport parameters of a pellet of $Sb_{1.7}Bi_{0.4}Te_{3.0}$ nanoplatelets as compared to bulk $Sb_{1.5}Bi_{0.5}Te_{3.0}$ ingots. (Right) "PGEC-factor" (the ratio of relative electric to total thermal conductivity) of $Sb_{1.7}Bi_{0.4}Te_{3.0}$ nanoplatelets.

lets show a positive $\Delta\sigma/\Delta T$ ratio. This behavior has recently been predicted by Nolas and co-workers for nanostructured materials where transport properties are dominated by *grain boundary potential barrier scattering* in combination with phonon scattering.[34] At not too low temperatures, electric transport across the grain boundaries can be described by thermionic emission with $\sigma(T) \sim T^{-1/2} \exp[-E_B/kT]$, where E_B is the height of the grain boundary potential barrier. Thus, for certain temperatures and grain boundary potential barriers, $\Delta\sigma/\Delta T$ can become positive. This is an important difference to bulk $Sb_{1.5}Bi_{0.5}Te_3$, where the negative $\Delta\sigma/\Delta T$ ratio forces a maximum in ZT at 50 °C preventing an efficient application at significantly higher temperatures.

The positive thermopower (Figure 4b) indicates p-type behavior in accordance with other $Sb_{1.5}Bi_{0.5}Te_3$ materials. The magnitude of, at best, 175 $\mu V\ K^{-1}$ is lower than that of comparable materials by other groups, which can reach up to 220 $\mu V\ K^{-1}$. Like no other thermoelectric parameter, S varies strongly with the chemical composition. For example, for the nanosheets displayed in Figure 1a,c,e, with a composition of $Sb_{1.0}Bi_{1.0}Te_{3.0}$ (see Figure 2b), we find a thermopower of merely 30 $\mu V\ K^{-1}$. We note that the composition of the nanoplatelets is with $Sb_{1.7}Bi_{0.4}Te_{3.0}$, too rich in antimony to fully compete with the optimized $Sb_{1.5}Bi_{0.5}Te_{3.0}$ samples applied in other works showing the best thermopower values. We believe that further optimization of our synthesis toward this ideal chemical composition will also lead to thermopower values of up to 220 $\mu V\ K^{-1}$. The precondition that the thermopower of nanostructured materials can be at least as high as in single crystals has been verified by several other groups already.[35−38]

The combination of the two parameters to the power factor (σS^2, Figure 4c) leads to an unusual temperature dependence. In bulk samples, σS^2 decreases with T at not too low temperatures, owing to the negative $\Delta\sigma/\Delta T$ ratio. In contrast, for the material in this work, $\sigma S^2(T)$ increases with temperature since $\Delta\sigma/\Delta T$ is positive.

Consequently, ZT(T) (Figure 4d) also increases with temperature. Starting with a moderate $ZT_{25\ °C} = 0.5$, at the highest measurement temperature we find $ZT_{145\ °C} = 0.9$, which is 15% larger than that of a comparable bulk material. A maximum in ZT can be estimated to be found significantly above 145 °C when thermopower begins to be depleted by bipolar conduction and other effects. This is in agreement with other reports that translated the maximum in ZT of bulk $SbBiTe_3$ at 50 °C to about 100 °C *via* nanostructuring.[3,26,35] The present work demonstrates the continuation of this trend probably due to the introduction of larger *grain boundary potential barriers*, which has been shown to drastically alter electron transport. This needs to be verified in the future *via* Hall mobility measurements.

In Figure 5 (left), the reason for the enhanced thermoelectric efficiency is summarized. By fitting the experimental data on the transport properties of bulk and nanostructured $Sb_{(2-x)}Bi_xTe_3$ from Figures 3c,d and 4a, we plot the relative reduction of σ, κ, and κ_L as a function of T resulting from the material's nanostructure. Over the entire temperature range, the reduction in κ is larger than the reduction in σ. As mentioned above, this is the key requirement for designing more efficient thermoelectric materials.

It is noteworthy that the relative reduction of κ is with 60% practically constant over the entire temperature regime. This is the result of the increased relative electric conductivity in combination with a simultaneous decrease in the relative lattice thermal conductivity. Materials with this behavior are often referred to as "*phonon-glass electron-crystals*" (PGEC), meaning materials with good charge carrier but poor phonon transport.

In Figure 5 (right) we introduce the temperature-dependent "PGEC factor" defined as the ratio of the relative electric to total thermal conductivity compared to the bulk state. For the pellets of $Sb_{1.7}Bi_{0.4}Te_{3.0}$ nanoplatelets in this communication, the PGEC factor starts at almost unity at room temperature but increases quickly to 1.8 at 140 °C. Provided the thermopower can be improved to the bulk value by adjusting the chemical composition to $Sb_{1.5}Bi_{0.5}Te_{3.0}$, the PGEC factor is a direct measure ($ZT_{nano} = ZT_{bulk} \times$ PGEC factor) for the expected improvement in ZT as compared to the bulk material. This way, ZT = 1.5 is within reach.

CONCLUSION

We have demonstrated the applicability of ligand supported, bottom-up synthesized $Sb_{(2-x)}Bi_xTe_3$ nanoplatelets for highly efficient, macroscopic, p-type thermoelectric materials. The enhancement in ZT is achieved by the *phonon-glass electron-crystal* effect, which describes the preferential scattering of phonons as compared to electrons by the nanostructure. The key to this property is a reduction in the lattice (or phononic) thermal conductivity leading to an enhancement in ZT by up to 15% as compared to comparable bulk materials. Future adjustments of the chemical composition hold for an enhancement of up to 80%. The maximum in ZT is shifted to larger temperatures which seems to be a direct consequence of the nanostructure.

METHODS

All manipulations were carried out under an inert atmosphere using standard Schlenck techniques if not stated otherwise.

I. Preparation of a 0.500 M Solution of Tellurium in TOP (Te@TOP). In a glovebox, tellurium (1.276 g, 10.00 mmol, 99.999%, Chempur) and tetradecylphosphonic acid (102 mg, Alfa Aesar) were suspended in distilled TOP (20.0 mL, 90%, Merck) under stirring. It was heated stepwise to 230 °C from room temperature by increasing the temperature by approximately 50 °C every 30 min. The final temperature was kept until a completely transparent, orange solution was obtained, which turned to bright-yellow on cooling to room temperature. The solution was stored in the glovebox.

II. Synthesis of $Sb_{1.0}Bi_{1.0}Te_{3.0}$ Nanosheets. In a typical synthesis, bismuth acetate (0.045 g, 0.12 mmol, 99% Aldrich) and antimony acetate (0.323 g, 1.08 mmol, 99% Aldrich) were mixed with 1-dodecanethiol (13.3 mL, 98% Aldrich) and heated to 45 °C for 45 min under vacuum on which a transparent, yellow solution was obtained. The flask was flooded with nitrogen, set to ambient pressure, and was heated to 60 °C, in which oleylamine (26.7 mL, 70%, Aldrich) was quickly added under stirring (referred to as *slow reduction* in the main body of the paper). After 3 min, when the solution had visibly darkened, 3.6 mL of Te@TOP were injected under vigorous stirring (referred to as *fast reduction* in the main body of the paper). After 24 h, the as-prepared $Sb_{1.0}Bi_{1.0}Te_{3.0}$ nanosheets were ready for further manipulations.

III. Synthesis of $Sb_{1.7}Bi_{0.4}Te_{3.0}$ Nanoplatelets. The amounts and procedure were identical to **(II)**, with the only alteration being the reaction temperature, which was 90 °C instead of 60 °C.

IV. Purification of $Sb_{(2-x)}Bi_xTe_3$ Nanosheets or Nanoplatelets for Characterization. A fraction of the dark-gray suspension obtained under **(II)** or **(III)** was mixed with ethanol (25 vol %, analytical grade, Fluka) and centrifuged at 4500 rpm for 5 min. The light yellow supernatant was removed under nitrogen and the almost black precipitate suspended in a few drops of chloroform (analytical grade, Fluka) on which the washing cycle was repeated two more times. The purified nanosheets or nanoplatelets should be stored in the absence of oxygen to prevent aging.

V. Ligand Removal from $Sb_{(2-x)}Bi_xTe_3$ Nanosheets or Nanoplatelets. The purified **(II)** or **(III)** were precipitated again with ethanol, and the supernatant was removed after centrifugation. The black precipitate was mixed with a large excess of oleic acid (~3 mL, 90%, Aldrich), allowed to stir overnight,and a black suspension was formed. The supernatant was removed after a short centrifugation and fresh oleic acid was added in which the mixture was allowed to stir for several hours. The supernatant was removed again after centrifugation and it was washed three times with hexane (analytical grade, Aldrich). The precipitate was suspended in a solution of NH_3 in methanol (2 mL, 7 mol L^{-1}, Aldrich). After stirring overnight, the supernatant was removed after centrifugation (4500 rpm, 5 min) and was washed two times with fresh NH_3 in methanol followed by three washing steps with hexane. All solvents were removed, it was dried under vacuum overnight, and a fine black powder was obtained. Typically, the starting amounts specified under **(II)** yield approximately 100 mg of $Sb_{1.0}Bi_{1.0}Te_{3.0}$ nanosheets and 180 mg of $Sb_{1.7}Bi_{0.4}Te_{3.0}$ nanoplatelets for **(III)**.

VI. Compaction of $Sb_{(2-x)}Bi_xTe_3$ Nanoplatelet Pellets by Spark Plasma Sintering. Typically, 95 mg of **(V)** kept under argon were loaded into a WC/Co die of 8.0 × 1.5 mm in area. The powder was pressed to a solid pellet of equal dimensions and approximately 1.4 mm in height by spark plasma sintering in a SPS-515 ET/M apparatus (Dr. Sinterlab). For thermal conductivity measurements, 165 mg of **(V)** were loaded into a disk-shaped die of 6 mm in diameter to obtain a tablet of $Sb_{(2-x)}Bi_xTe_3$ nanosheets 1.3 mm in height. On applying 340 MPa (for rectangular bars) or 530 MPa (for disks) pressure, the die containing the nanopowder was heated from 20 to 50 °C in 5.0 min with a 10.0 min hold time by applying a DC current between 0 and 165 A and immediately allowed to cool down to room temperature. The obtained $Sb_{(2-x)}Bi_xTe_3$ pellets of nanoplatelets were mechanically robust and silver−metallic in appearance.

(HR-)TEM imaging was performed with a JEOL JEM 2200 FS (UHR) with CESCOR and CETCOR corrector at an acceleration voltage of 200 kV or a JEM-Jeol-1011 microscope at 100 kV with a CCD camera. SEM images were obtained on a LEO1550 scanning electron microscope with a spatial resolution of ~1 nm. XRPDs were recorded using a Philipps X'Pert-diffractometer with Bragg−Brentano geometry on applying Cu Kα radiation (λ = 154.178 pm, U = 45 kV; I = 40 mA).

For measurements of the thermopower and resistivity, a ZEM-3 apparatus (ULVAC-RIKO) was applied under a low-pressure helium atmosphere. The thermopower was determined by a static dc method where the resistivity was simultaneously measured by a four-terminal setup.

The specific heat was measured by a relaxation technique in a Physical Property Measurement System by Quantum Design. A heat pulse of 2% of the bath temperature has been applied and repeated three times at each temperature.

Thermal diffusivity measurements were recorded with a Netzsch LFA-441 and a Netzsch LFA-457 Microflash with a Pyroceram standard for calibration.

ICP-OES analysis was performed with a Spectro Ciros CCD (Spectro Analytical Instruments) subsequent to powder sample digestion in a microwave assisted sample decomposition system (MARS 5, CEM Corporation) with a mixture of 20% nitric acid and tartaric acid (L(+)-tartaric acid, p.a., 99.5%, Sigma-Aldrich). The latter proved necessary as complexing agent to overcome the formation of insoluble Sb_2O_3. The bismuth, antimony, and tellurium contents were determined by calibration with matrix matched solutions produced form ICP standard solutions (1000 mg L^{-1} Bi, $Bi(NO_3)_3$ in HNO_3 2−3%, Merck, 1000 mg L^{-1} Sb, Sb_2O_3 in HCl 7%, Merck, 1000 mg L^{-1} Te, H_6TeO_6 in HNO_3 2−3%, Merck). The relative errors of the analysis by ICP-OES were <3.7%.

Acknowledgment. We thank Katrin Meier for help with SPS experiments, William Töllner for help with DSC measurements and Michael Baitinger for fruitful discussions. A Ph.D. grant by the *Studienstiftung des deutschen Volkes* is gratefully acknowledged.

Supporting Information Available: TEM image of nanoflakes (Figure S1); XRPD of $Sb_{1.0}Bi_{1.0}Te_{3.0}$ nanosheets (Figure S2); EDX spectrum of $Sb_{1.7}Bi_{0.4}Te_{3.0}$ nanoplatelets (Figure S3); XRPD of $Sb_{1.7}Bi_{0.4}Te_{3.0}$ nanoplatelets before and after ligand exchange (Figure S4); Temperature−time profile of SPS experiments (Figure S5); Photograph of nanostructured bulk samples (Figure S6) and XRPD after SPS sample fabrication (Figure S7); Investigation of anisotropy in structure and thermal transport (Figure S8). This material is available free of charge *via* the Internet at http://pubs.acs.org.

REFERENCES AND NOTES

1. Goldsmid, H. J.; Douglas, R. W. The Use of Semiconductors in Thermoelectric Refrigeration. *Brit. J. Appl. Phys.* **1954**, *5*, 386–390.
2. Ettenberg, M. H.; Jesser, W. A.; Rosi, F. D. A New n-Type and Improved p-Type Pseudo-Ternary $(Bi_2Te_3)(Sb_2Te_3)(Sb_2Se_3)$ Alloy for Peltier Cooling. Proceedings of 15th International Conference on Thermoelectrics, Pasadena, California, March 26−29, Caillat, T., Ed.; IEEE, Piscataway, NJ, 1996; pp 52−56.
3. Poudel, B.; Hao, Q.; Ma, Y.; Lan, Y.; Minnich, A.; Yu, B.; Yan, X.; Wang, D.; Muto, A.; Vashaee, D. High Thermoelectric Performance of Nanostructured Bismuth Antimony Telluride Bulk Alloys. *Science* **2008**, *320*, 634–638.
4. Xie, W.; Tang, X.; Yan, Y.; Zhang, Q.; Tritt, T. M. High Thermoelectric Performance BiSbTe Alloy with Unique Low-Dimensional Structure. *J. Appl. Phys.* **2009**, *105*, 113713–8.
5. Venkatasubramanian, R.; Siiwvola, E.; Colpitts, T.; O'Quinn, B. Thin-Film Thermoelectric Devices with High Room-Temperature Figures of Merit. *Nature* **2001**, *413*, 597–602.
6. Lan, Y.; Poudel, B.; Ma, Y.; Wang, D.; Dresselhaus, M. S; Chen, G.; Ren, Z. Structure Study of Bulk Nanograined Thermoelectric Bismuth Antimony Telluride. *Nano Lett.* **2009**, *9*, 1419–22.
7. Dirmyer, M. R.; Martin, J.; Nolas, G. S.; Sen, A.; Badding, J. V. Thermal and Electrical Conductivity of Size-Tuned Bismuth Telluride Nanoparticles. *Small* **2009**, *5*, 933–37.
8. Lan, Y.; Minnich, A. J.; Chen, G.; Ren, Z. Enhancement of Thermoelectric Figure-of-Merit by a Bulk Nanostructuring Approach. *Adv. Funct. Mater.* **2010**, *20*, 357–76.
9. Zhao, Y.; Burda, C. Chemical Synthesis of $Bi_{0.5}Sb_{1.5}Te_3$ Nanocrystals and Their Surface Oxidation Properties. *ACS Appl. Mater. Int.* **2009**, *1*, 1259–63.
10. Wang, R. Y.; Feser, J. P.; Lee, J.-S.; Talapin, D. V.; Segalman, R.; Majumdar, A. Enhanced Thermopower in PbSe Nanocrystal Quantum Dot Superlattices. *Nano Lett.* **2008**, *8*, 2283–88.
11. Scheele, M.; Oeschler, N.; Meier, K.; Kornowski, A.; Klinke, C.; Weller, H. Synthesis and Thermoelectric Characterization of Bi_2Te_3 Nanoparticles. *Adv. Funct. Mater.* **2009**, *19*, 3476–83.
12. Glatz, A.; Beloborodov, I. S. Thermoelectric Properties of Granular Metals. *Phys. Rev. B* **2009**, *79*, 041404-8 (R).
13. Popescu, A.; Woods, L. M.; Martin, J.; Nolas, G. S. Model of Transport Properties of Thermoelectric Nanocomposite Materials. *Phys. Rev. B* **2009**, *79*, 205302-7.
14. Zebarjadi, M.; Esfarjani, K.; Shakouri, A.; Bahk, J.-H.; Bian, Z.; Zeng, G.; Bowers, J.; Lu, H.; Zide, J.; Gossard, A. Effect of Nanoparticle Scattering on Thermoelectric Power Factor. *Appl. Phys. Lett.* **2009**, *94*, 202105-3.
15. Zhang, H; Liu, C.-X.; Qi, X.-L.; Dai, X.; Fang, Z.; Zhang, S.-C. Topological Insulators in Bi_2Se_3, Bi_2Te_3 and Sb_2Te_3 with a Single Dirac Cone on the Surface. *Nat. Phys.* **2009**, *5*, 438–442.
16. Chiritescu, C.; Mortensen, C.; Cahill, D. G.; Johnson, D.; Zschack, P. Lower Limit to the Lattice Thermal Conductivity of Nanostructured Bi_2Te_3-Based Materials. *J. Appl. Phys.* **2009**, *106*, 073503-5.
17. Teweldebrhan, D; Goyal, V; Balandin, A. A. Exfoliation and Characterization of Bismuth Telluride Atomic Quintuples and Quasi-Two-Dimensional Crystals. *Nano Lett.* **2010**, *10*, 1209–1218.
18. Kong, D.; Dang, W.; Cha, J., J.; Li, H.; Meister, S.; Peng, H.; Liu, Z.; Cui, Y. Few-Layer Nanoplates of Bi_2Se_3 and Bi_2Te_3 with Highly Tunable Chemical Potential. *Nano Lett.* **2010**, *10*, 2245–2250.
19. Lu, W.; Ding, Y.; Chen, Y.; Wang, Z. L.; Fang, J. Bismuth Telluride Hexagonal Nanoplatelets and Their Two-Step Epitaxial Growth. *J. Am. Chem. Soc.* **2005**, *127*, 10112–16.
20. Wang, W.; Poudel, B.; Yang, J.; Wang, D. Z.; Ren, Z. F. High-Yield Synthesis of Single-Crystalline Antimony Telluride Hexagonal Nanoplates Using a Solvothermal Approach. *J. Am. Chem. Soc.* **2005**, *127*, 13792–93.
21. Rupp, J; Birringer, R. Enhanced Specific Heat Capacity (c_P) Measurements (150−300 K) of Nanometer-Sized Crystalline Materials. *Phys. Rev. B* **1987**, *36*, 7888–7890.
22. Scheele, M.; Oeschler, N.; Meier, K.; Kornowski, A.; Klinke, C.; Weller, H. Colloidal Nanostructures as Building Blocks for Macroscopic Thermoelectric Materials with Electron-Crystal Phonon-Glass Properties. In *Thermoelectric Materials—Growth, Properties, Novel Characterization Methods, and Applications*; Tuller, H. L., Baniecki, J. D., Snyder, G. J., Malen, J. A., Eds.; Mater. Res. Soc. Symp. Proc. 1267: Warrendale, PA, 2010; DD-08-12.
23. Shrivastava, K. N. Specific Heat of Nanocrystals. *Nano Lett.* **2002**, *2*, 21–24.
24. Zhu, Y. F.; Lian, J. S.; Jiang, Q. Modelling of the Melting Point, Debye Temperature, Thermal Expansion Coefficient, and the Specific Heat of Nanostructured Materials. *J. Phys. Chem. C* **2009**, *113*, 16896–16900.
25. Fleurial, J. P.; Gailliard, L.; Triboulet, R.; Scherrer, H.; Scherrer, S. Thermal Properties of High Quality Single Crystals of Bismuth Telluride Part I: Experimental Chracterization. *J. Phys. Chem. Solids* **1988**, *49*, 1237–47.
26. Ma, Y.; Hao, Q.; Poudel, B.; Lan, Y.; Yu, B.; Wang, D.; Chen, G.; Ren, Z. Enhanced Thermoelectric Figure-of-Merit in p-Type Nanostructured Bismuth Antimony Tellurium Alloys Made from Elemental Chunks. *Nano Lett.* **2008**, *8*, 2580–84.
27. Yang, L.; Wu, J. S.; Zhang, L. T. Synthesis of Filled Skutterudite Compound $La_{0.75}Fe_3CoSb_{12}$ by Spark Plasma Sintering and Effect of Porosity on Thermoelectric Properties. *J. Alloys Compd.* **2004**, *364*, 83–88.
28. Cao, Y. Q.; Zhu, T. J.; Zhao, X. B. Low Thermal Conductivity and Improved Figure of Merit in Fine-Grained Binary PbTe Thermoelectric Alloys. *J. Phys. D* **2009**, *42*, 015406-6.
29. Adachi, J.; Kurosaki, K.; Uno, M.; Yamanaka, S. Effect of Porosity on Thermal and Electrical Properties of Polycrystalline Bulk ZrN Prepared by Spark Plasma Sintering. *J. Alloys Compd.* **2007**, *432*, 7–10.
30. Gesele, G.; Linsmeier, J.; Drach, V.; Fricke, J.; Arens-Fischer, R. Temperature-Dependent Thermal Conductivity of Porous Silicon. *J. Phys. D* **1997**, *30*, 2911–16.
31. Sumirat, I.; Ando, Y.; Shimamura, S. Theoretical Consideration of the Effect of Porosity on Thermal Conductivity of Porous Materials. *J. Porous Mater.* **2006**, *13*, 439–443.
32. Seto, J. Y. W. The Electrical Properties of Polycrystalline Silicon Films. *J. Appl. Phys.* **1975**, *46*, 5247–54.
33. Kamins, T. I. Hall Mobility in Chemically Deposited Polycrystalline Silicon. *J. Appl. Phys.* **1971**, *42*, 4357–65.
34. Martin, J.; Wang, L.; Chen, L.; Nolas, G. S. Enhanced Seebeck Coefficient through Energy-Barrier Scattering in PbTe Nanocomposites. *Phys. Rev. B* **2009**, *79*, 115311-5.
35. Cao, Y. Q.; Zhao, X. B.; Zhu, T. J.; Zhang, X. B.; Tu, J. P. Synthesis and Thermoelectric Properties of Bi_2Te_3/Sb_2Te_3 Bulk Nanocomposites with Laminated Nanostructure. *Appl. Phys. Lett.* **2008**, *92*, 143106-3.
36. Yu, F.; Zhang, J.; Yu, D.; He, J.; Liu, Z.; Xu, B.; Tian, Y. Enhanced Thermoelectric Figure of Merit in Nanocrystalline Bi_2Te_3 Bulk. *J. Appl. Phys.* **2009**, *105*, 094303-5.
37. Zhao, L.-D.; Zhang, B.-P.; Liu, W.-S.; Li, J.-F. Effect of Mixed Grain Sizes on Thermoelectric Performance of Bi_2Te_3 Compound. *J. Appl. Phys.* **2009**, *105*, 023704-6.
38. Gothard, N.; Ji, X.; He, J.; Tritt, T. M. Thermoelectric and Transport Properties of *n*-Type Bi_2Te_3 Nanocomposites. *J. Appl. Phys.* **2008**, *103*, 054314-4.